

Disentangled Latent Energy-Based Style Translation: An Image-Level Structural MRI Harmonization Framework

Mengqi Wu^{a,b}, Lintao Zhang^a, Pew-Thian Yap^a, Hongtu Zhu^c, Mingxia Liu^{a,*}

^aJoint Department of Biomedical Engineering, University of North Carolina at Chapel Hill and North Carolina State University, Chapel Hill, NC 27599, USA

^bDepartment of Radiology and BRIC, University of North Carolina at Chapel Hill, Chapel Hill, NC 27599, USA

^cDepartment of Biostatistics and Biomedical Research Imaging Center, University of North Carolina at Chapel Hill, NC 27599, USA

Abstract

Brain magnetic resonance imaging (MRI) has been extensively employed across clinical and research fields, but often exhibits sensitivity to *site effects* arising from non-biological variations such as differences in field strength and scanner vendors. Numerous retrospective MRI harmonization techniques have demonstrated encouraging outcomes in reducing the site effects at image level. However, existing methods generally suffer from high computational requirements and limited generalizability, restricting their applicability to unseen MRIs. In this paper, we design a novel disentangled latent energy-based style translation (DLEST) framework for unpaired image-level MRI harmonization, consisting of (1) *site-invariant image generation* (SIG), (2) *site-specific style translation* (SST), and (3) *site-specific MRI synthesis* (SMS). Specifically, the SIG employs a latent autoencoder to encode MRIs into a low-dimensional latent space and reconstruct MRIs from latent codes. The SST utilizes an energy-based model to comprehend global latent distribution of a target domain and translate source latent codes toward the target domain, while SMS enables MRI synthesis with a target-specific style. By disentangling image generation and style translation in latent space, the DLEST can achieve efficient style translation. Our model was trained on T1-weighted MRIs from a public dataset (with 3,984 subjects across 58 acquisition sites/settings) and validated on an independent dataset (with 9 traveling subjects scanned in 11 sites/settings) in 4 tasks: (1) histogram and clustering comparison, (2) site classification, (3) brain tissue segmentation, and (4) site-specific MRI synthesis. Qualitative and quantitative results demonstrate the superiority of our method over several state-of-the-arts.

Keywords: MRI harmonization, Style translation, MRI synthesis, Energy-based model

1. Introduction

Structural magnetic resonance imaging (MRI) has found extensive application in both clinical diagnostics and research studies, primarily due to its ability to offer high spatial resolution in a non-invasive manner (Evans et al., 2020; Albayram et al., 2022; Varela et al., 2017). Large-scale data initiatives and neuroimaging studies often utilize brain MRI data pooled from various acquisition

sites/settings to enhance subject cohort and boost statistical power of learning models (An et al., 2022; Tofts and Collins, 2011; Schnack et al., 2010). However, models directly trained on these multi-site datasets often encounter difficulties in achieving convergence (Glocker et al., 2019; Sun et al., 2021) and in generalizing to new data, due to the sensitivity of MRI to non-biological variations, known as *site effects*. The site effect can be attributed to a variety of factors, including differences in field strengths, scanner vendors, scanning protocols, and hardware upgrade and maintenance. (Glocker et al., 2019; Wachinger et al.,

*Corresponding author: M. Liu (mingxia.liu@med.unc.edu).

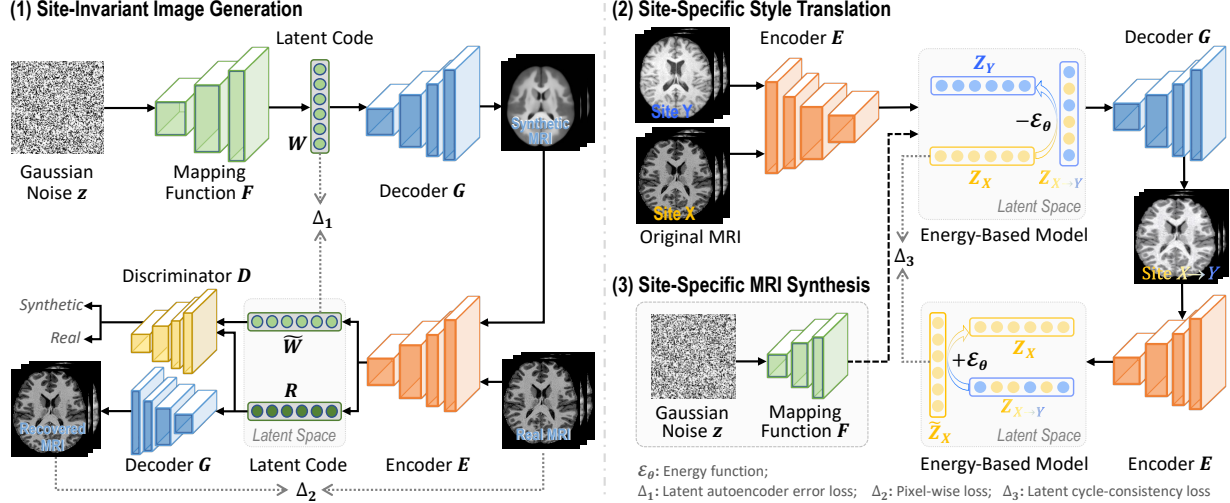


Figure 1: The proposed disentangled latent energy-based style translation (DLEST) framework for MRI harmonization at the image level, consisting of (1) *site-invariant image generation* that encodes images into low-dimensional latent space and reconstruct images based on latent codes, (2) *site-specific style translation* that facilitates implicit style translation within the latent space, and (3) *site-specific MRI synthesis* that generates diverse synthetic MRIs with a given target site style.

2021; Helmer et al., 2016). While multi-site studies, such as Alzheimer’s Disease Neuroimaging Initiative (Jack Jr et al., 2008), aim to mitigate the site effects during data acquisition through unified scanning protocols, certain variations are still inevitable, like those caused by scanner maintenance and software upgrades. Additionally, many studies rely on the retrospective pooling of multi-site data, when there was no coordination among different sites during image acquisition (Dufumier et al., 2022). One possible solution to address such a challenge is to retrospectively harmonize the imaging data as a preprocessing step (Cackowski et al., 2023; Zuo et al., 2021).

Existing methods for MRI harmonization can generally be classified into two categories: (1) *feature-level* and (2) *image-level* approaches. Feature-level techniques, such as ComBat (Johnson et al., 2007) and ComBat-GAM (Pomponio et al., 2020), typically utilize empirical Bayes models and pre-extracted biological or radiomic features from a set of pre-defined regions-of-interest (ROIs). Nonetheless, the effectiveness of these methods is largely contingent on the size of datasets and the quality of feature extraction, which restricts their versatility across applications that employ diverse MRI features (Cackowski et al., 2023; An et al., 2022). On the other hand, image-level harmonization is designed for a wider range of down-

stream applications and is not reliant on pre-defined MRI features, which is the primary objective of this paper.

For image-level harmonization, many deep generative models have been employed in recent studies (Zhu et al., 2017; Choi et al., 2020; Liu et al., 2021; Zuo et al., 2021; Cackowski et al., 2023). These methods, rather than harmonizing a set of pre-extracted MRI features, approach the harmonization problem as a pixel-to-pixel translation task at the image level. The objective is to alter the style of a source MRI to match a target MRI while preserving the original content. In this context, the *style information* refers to high-level features like intensity difference, contrast variations, and signal-to-noise ratio, while *content information* pertains to low-level image features such as anatomical structures, contours, and edges. Several state-of-the-art (SOTA) methods utilize generative adversarial networks (GANs) for image-level MRI harmonization. For instance, CycleGAN (Zhu et al., 2017) imposes cycle-consistency constraints in its loss function to enforce content preservation during unpaired style translation. StarGAN (Choi et al., 2020) employs separate encoders to learn site-specific style codes and injects them into images via adaptive instance normalization. ImU- nity (Cackowski et al., 2023) incorporates additional en- coder networks as extra constraints for learning latent rep-

representations to remove the site bias and retain clinical information. In addition to GAN-based models, some recent works utilize encoder-decoder models to learn disentangled latent representations for anatomical structure and contrast to perform image-level MRI harmonization (Zuo et al., 2022; Dewey et al., 2020). However, existing image-level methods usually utilize deep networks to separately learn style and content encoding in image space, leading to significantly increased training time and computational cost due to the optimization of numerous network parameters (Gulrajani et al., 2017). Furthermore, many approaches need to retrain their models entirely when applied to unseen MRI data, therefore limiting their practical generalizability (Cackowski et al., 2023).

In this paper, we propose a novel disentangled latent energy-based style translation (**DLEST**) framework for unpaired structural MRI harmonization at the image level. As illustrated in Fig. 1, the DLEST includes (1) a *site-invariant image generation* module, using a latent autoencoder for encoding and generating MRIs from a lower-dimensional latent space, (2) a *site-specific style translation* module, using an energy-based model for implicit style translation through latent space, and (3) a *site-specific MRI synthesis* module for generating synthetic MRI scans with given site-specific styles. Through the disentanglement of image generation and style translation in latent space, the DLEST can achieve efficient and generalizable MRI harmonization. It can also be extended to synthesize MRIs with site-specific styles and diverse anatomical details, without extra model training.

An initial version of our work has been introduced in MLMI 2023 (Wu et al., 2023). This journal paper introduces several advancements, including 1) extension of our framework for site-specific MRI synthesis, with qualitative and quantitative evaluations, 2) a thorough literature review on image-level harmonization methods and the application of energy-based models for generation tasks, 3) adding comparison with a recent state-of-the-art method, 4) experimentation with specific loss functions for content and style regularization, 5) adding comparative visualization of brain tissue segmentation results, and 6) adding quantitative comparison of computational cost across all learning methods.

The key contributions of this work are outlined as follows.

- We propose a novel disentangled latent energy-based style translation framework for unpaired MRI harmonization at the image level, achieving more computationally efficient style translation in low-dimensional latent space.
- Our framework can generalize to new data without model retraining since the image generation module can directly encode and reconstruct MRIs without site specification. Once trained for harmonization, our framework can natively synthesize MRIs with style of a specified site.
- We incorporate an energy-based model to capture the latent data distribution of target MRI scans for harmonization. This enables our model to more effectively account for intra-site variations within the target domain and avoids pre-defining a reference image for harmonization.
- Our framework is rigorously evaluated on two public datasets with T1-weighted MRIs across four tasks, with qualitative and quantitative results underscoring the superiority of our DLEST over SOTA methods.

2. Related Work

2.1. Image-Level MRI Harmonization

Inspired by the image-to-image translation task in the natural imaging domain, recent studies have employed the generative adversarial network (GAN) models to tackle medical data harmonization problems on the image level (Zhu et al., 2017; Choi et al., 2020; Liu et al., 2021). These methods engage the generator and discriminator networks in an adversarial game, where the generator creates synthetic images resembling the real dataset distribution, and the discriminator differentiates between synthetic and real images (Zhu et al., 2017). For instance, CycleGAN introduces a cycle-consistency constraint in its loss function for unpaired image translation and content (anatomical structure) preservation (Zhu et al., 2017). Style-encoding GAN (Liu et al., 2021), inspired by StarGAN-V2 (Choi et al., 2020), further separates the content and style encoding in the latent space, allowing the site-specific style code to be learned and injected into images via adaptive instance normalization. ImUnity (Cackowski et al., 2023) modifies the GAN

structure by adding a site/scanner unlearning module to encourage the encoder to learn domain-invariant latent representations. These advancements have contributed to the continual improvement of GAN-based harmonization methods.

In addition to GAN-based models, recent studies have introduced an alternative approach that employs encoder-decoder networks to disentangle anatomical and contrast information in latent space. For instance, CALAMITI (Zuo et al., 2021) first uses T1- and T2-weighted (T1/T2-w) MRI pairs to learn global latent codes containing anatomical and contrast information, and then disentangles style and content latent codes via separate encoders and decoders. Similarly, Dewey *et al.* (Dewey et al., 2020) leverage T1-w and T2-w image pairs to attain a disentangled latent space, comprising high-resolution anatomical and low-dimensional contrast components via a Randomization block. This block allows generating MRIs with identical anatomical structures but varying contrast. Zuo *et al.* (Zuo et al., 2022) enhance this approach by ablating the need for paired MRI sequences. Instead, they employ 2D slices from axial and coronal views of the same MRI to provide the same contrast but different anatomical information.

These existing methods usually involve simultaneous training of multiple encoders, decoders, or sub-networks for separated style and content encoding, resulting in increased computational and time costs for model training. Besides, some methods have limited generalizability on new MRI as their models need to be retrained entirely on new datasets. Moreover, certain existing studies necessitate paired MRI scans for model training, like traveling subjects or multiple sequences, which are often unavailable in practice. In this work, we aim to enhance the efficiency of image-level harmonization and the model’s generalizability to new data, while also expanding its capacity for site-specific image synthesis.

2.2. Energy-Based Models for Image Generation

Generative models are a type of probabilistic model, which models a joint probability of the observed data and the target data. For the image generation task, a model observes image samples or their latent representations and learns to capture the true data distribution to generate new images that resemble the observed samples (Pang et al., 2020; Du and Mordatch, 2019). Probabilistic models

employ statistical inference methods, such as maximum likelihood estimation (MLE), to estimate parameters that maximize the likelihood of the observed data under an assumed distribution (Ng and Jordan, 2001). However, these models need to be correctly normalized. This process can sometimes involve the evaluation of intractable integrals over all possible variable configurations, which can be computationally challenging. Therefore, LeCun *et al.* (LeCun et al., 2006) use energy-based learning as an alternative framework for both discriminative and generative tasks. Energy-based models (EBMs) capture data dependencies by associating a scalar energy value (a measure of compatibility) to each configuration of variables (LeCun et al., 2006). Unlike probabilistic models, EBMs do not require normalization. For generative tasks, the training phase of EBMs involves learning an appropriate energy function that assigns low energy values to observed data within the real data distribution and high energy values otherwise, during which data is typically sampled via Markov Chain Monte Carlo (MCMC) sampling methods. During inference, the EBMs generate data by exploring the energy surface to sample configurations that minimize the energy function.

Over the years, many studies have employed EBMs for image generation and improved on various aspects. Du *et al.* (Du and Mordatch, 2019) propose to utilize Langevin Dynamics, a gradient-based MCMC method, for more efficient sampling and mixing on high-dimensional image domains. Pang *et al.* (Pang et al., 2020) further improve the sampling efficiency and the MCMC mixing by combining an EBM with a top-down network (decoder) in the low-dimensional latent space. The EBM serves to refine the simple isotropic Gaussian prior to be closer to the data distribution, leading to improved quality during image generation. Xiao *et al.* (Xiao et al., 2020) propose a symbiosis of Variational Autoencoder (VAE) and EBM to leverage the advantages of both. The VAE captures the overall model structure of the data distribution and provides an improved latent initialization of the MCMC sampling, which is used in EBM. The EBM, on the other hand, can exclude non-data-like samples and refine the latent representation for VAE to decode. A recent work (Zhao and Chen, 2021) utilizes this symbiotic combination of EBM and autoencoder for the task of male-to-female face translation. In this context, the EBM learns the latent distribution of a target image domain and trans-

lates the source latent representation towards this target distribution. The underlying assumption is that two image domains share certain common latent representations. The EBM is then able to implicitly translate latent codes that encapsulate domain differences while preserving shared latent codes that signify domain similarities. Inspired by the success of EBMs in natural image-to-image translation, our method adopts a similar assumption. We posit that MRIs from different domains share some common latent representations that convey content (anatomical) information. We propose training an EBM to translate the site-specific style information from one domain to another within a low-dimensional latent space.

3. Materials and Methodology

3.1. Materials and Image Preprocessing

3.1.1. Datasets

Our study utilizes two public datasets, including (1) Open Big Healthy Brains (OpenBHB) (Dufumier et al., 2022) and (2) Strategic Research Program for Brain Science (SRPBS) (Tanaka et al., 2021). Specifically, the OpenBHB, a large-scale brain MRI dataset, comprises 3,984 T1-weighted MRIs from healthy subjects acquired from over 58 centers globally. The SRPBS dataset contains 108 T1-weighted structural MRIs acquired from 9 healthy traveling subjects across 12 scanners/settings. In this work, MR scans of 9 subjects from 11 acquisition sites/settings in SRPBS are used, while one duplicated site (YC2) is removed. Further details can be found online^{1,2}.

3.1.2. Data Preprocessing

For these two datasets, each MRI scan undergoes minimal preprocessing using FSL ANAT pipeline (Smith et al., 2004), which encompasses bias field correction, brain extraction, and 9 degrees of freedom linear registration to the MNI-152 template with 1 mm isotropic resolution. Brain tissue segmentation is performed on SRPBS images using FSL FAST pipeline, with each brain segmented into white matter (WM), gray matter (GM), and cerebrospinal fluid (CSF). For each MRI from OpenBHB,

we selected 10 slices in axial view from the center of each MRI. For SRPBS with limited MRIs, we chose 15 slices from each volume. Additionally, all these 2D slices were zero-padded to have the size of 256×256 .

3.2. Proposed Methodology

3.2.1. Problem Formulation

In this work, we reformulate image-level MRI harmonization as a *domain-level translation* task, which is different from previous studies that treat each MRI scan as a unique domain and concentrate on individual source-to-reference image translation (Liu et al., 2021; Cackowski et al., 2023). In the context of multi-site MRI studies, we consider a single site or scanning setting for MRI acquisition as a unique domain. This is justified by numerous studies demonstrating that MRIs scanned in the same site under the same setting can exhibit intra-site variations that result in different styles within one domain (Deoni et al., 2008; Styner et al., 2002). Consequently, image-level translation using only one reference image may not account for these variations, failing to capture true data distributions of a site/domain. For the two datasets used in this work, we first compute the mean peak signal-to-noise ratio (PSNR) for each domain by averaging the PSNR values obtained from every unique pair of images within that same domain. We then designate the domain with minimal intra-site variations (highest PSNR) as the *target domain*, with the remaining site(s) as the *source domain(s)*. Overall, we aim to translate MRIs within a source domain X to have the imaging style (*i.e.*, non-biological variation) of MRIs in a target domain Y .

Specifically, our goal is to train a latent autoencoder that can map a source and a target MRI scan to their respective latent codes, denoted as $E: \{\mathbf{x} \in X, \mathbf{y} \in Y\} \rightarrow \{Z_x, Z_y\}$. In this context, a latent code $Z = \{S, C\}$ represents an MRI scan in low-dimensional space by implicitly encapsulating both a *style code* S and a *content code* C . The source style code S_x is then implicitly translated to become closer to the style code S_y of the target domain, while the content code C_x is preserved. This style translation process can be formulated through a mapping $T: Z_x = \{S_x, C_x\} \rightarrow Z_{x \rightarrow y} = \{S_y, C_x\}$, where $Z_{x \rightarrow y}$ represents the latent code of an MRI after translation. Subsequently, using the same autoencoder, we learn another mapping $G: Z_{x \rightarrow y} \rightarrow \tilde{\mathbf{y}}$. This latent-to-image space mapping decodes the

¹<https://baobablab.github.io/bhb/>

²<https://www.synapse.org/#!/Synapse:syn22317076/wiki/605026>

translated source latent code $Z_{x \rightarrow y}$ to generate an image $\tilde{\mathbf{y}}$ in the target domain. This image, preserving the content of \mathbf{x} and adopting the style of \mathbf{y} , serves as an effective translation from the source to the target domain. To achieve this, as depicted in Fig. 1, our DLEST consists of three disentangled modules: *site-invariant image generation*, *site-specific style translation*, and *site-specific MRI synthesis*. The specifics of these modules are introduced as follows.

3.2.2. Site-Invariant Image Generation (SIG)

As shown in the left panel of Fig. 1, the SIG is designed to encode MRI scans into a lower-dimensional latent space and subsequently decode reconstructed MRIs from these latent codes. Importantly, this process is trained *independently of any site specifications*, and thus, does not require any site labels or image pairs. Specifically, the SIG module takes as input a real MRI $\mathbf{x} \sim \mathbb{P}_{Data}$ and a random noisy image z drawn from a Gaussian distribution $\mathcal{N}(0, 1)$, where \mathbb{P}_{Data} denotes the real data distribution. A network F learns a deterministic mapping to convert z into a latent code (Pidhorskyi et al., 2020), represented as $\mathcal{W} = F(z)$. Following this, we further design a stochastic decoding network G to generate a synthetic MR image based on the latent code \mathcal{W} and an independent noise $\eta \sim \mathcal{N}(0, 1)$, represented as $\tilde{\mathbf{x}} = G(\mathcal{W}, \eta)$. A network E is then trained to encode the synthetic image $\tilde{\mathbf{x}}$ back into the latent space, resulting in a reconstructed latent code $\tilde{\mathcal{W}}$. This entire process can be symbolized as $\tilde{\mathcal{W}} = E(\tilde{\mathbf{x}}) = E \circ G \circ F(z)$, where the symbol \circ denotes function composition. The encoder E also can transform a real image \mathbf{x} into its corresponding latent code, denoted as $\mathcal{R} = E(\mathbf{x})$. Lastly, a latent discriminator, denoted as D , receives a latent code and produces a probability value that signifies whether the latent code is derived from a synthetic or real MRI. The networks F , G , E , and D are trained using an adversarial approach, enabling the SIG module to generate latent codes that closely resemble those derived from real MRIs. The latent code \mathcal{R} , derived from the real image, is also decoded back to a reconstructed image using the decoder G , aiming to preserve the content (e.g., anatomical structures) of the real MRI.

To uphold the symmetry of the encoder and decoder in latent space, we aim to ensure that $\mathcal{W} = \tilde{\mathcal{W}}$, accomplished by minimizing the following *latent autoencoder*

error loss:

$$\mathcal{L}_{lae}^{E,G} = \Delta_1(F \circ E \circ G \circ F) = \mathbb{E}_{z \sim \mathbb{P}_z} [\|F(z) - E \circ G \circ F(z)\|_2^2] \quad (1)$$

Through this process, the network pair E and G can be interpreted as a *latent autoencoder* that encodes and reconstructs the latent code \mathcal{W} . This differs from conventional autoencoders, which typically operate in high-dimensional image space (Kingma and Welling, 2013). The generation of images via autoencoding low-dimensional latent codes enhances computational efficiency.

In order to maintain the anatomical structure preservation of the latent autoencoder E and G , a *pixel-wise content loss* is introduced to compute the difference between the original real image \mathbf{x} and its reconstructed counterpart $\tilde{\mathbf{x}}$, as follows:

$$\mathcal{L}_{pix}^{E,G} = \Delta_2(\mathbf{x} \parallel \tilde{\mathbf{x}}) = \mathbb{E}_{\mathbf{x} \sim \mathbb{P}_{Data}} [\|\mathbf{x} - G \circ E(\mathbf{x})\|_1] \quad (2)$$

which motivates the model to minimize content change during MRI reconstruction. To generate faithful synthetic MRIs, we propose to jointly optimize F , G , E , and D through an *adversarial loss*, which is formulated as:

$$\mathcal{L}_{adv}^{E,D} = \Phi(D \circ E \circ G \circ F(z)) + \Phi(-D \circ E(\mathbf{x})) + R_{reg} \quad (3)$$

$$\mathcal{L}_{adv}^{F,G} = \Phi(-D \circ E \circ G \circ F(z)) \quad (4)$$

where Φ is the *softplus* function defined as $\Phi(t) = \log(1 + \exp(t))$, R_{reg} is a zero-centered gradient penalty term defined as $\frac{\gamma}{2} \mathbb{E}_{\mathbf{x} \sim \mathbb{P}_{Data}} [\|\nabla D \circ E(\mathbf{x})\|^2]$ (Pidhorskyi et al., 2020).

Overall, the final objective functions of SIG is as follows:

$$\min_{\{F,G\}} \max_{\{E,D\}} \mathcal{L}_{adv}^{E,D} + \mathcal{L}_{adv}^{F,G}, \quad \min_{\{E,G\}} \mathcal{L}_{lae}^{E,G} + \mathcal{L}_{pix}^{E,G} \quad (5)$$

3.2.3. Site-Specific Style Translation (SST)

As depicted in the upper right panel of Fig. 1, the proposed SST consists of (1) an autoencoder that includes the networks E and G trained in the SIG module, and (2) an energy-based model (EBM) that performs latent-space style translation. Given an MRI \mathbf{x} from source site X and an MRI \mathbf{y} from target site Y , the encoder E initially transforms them into their respective latent codes, denoted as $Z_x = E(\mathbf{x})$ and $Z_y = E(\mathbf{y})$, respectively. These latent codes are then input into the EBM, which produces the translated latent code $Z_{x \rightarrow y}$. This translated latent code is subsequently decoded by G to produce the translated MRI.

The EBM is also utilized to reverse-translate $Z_{x \rightarrow y}$, resulting in a recovered source latent code, denoted as \tilde{Z}_x . This reconstructed latent code is compared with the original Z_x to ensure the latent cycle-consistency, which prevents mode collapse during the unpaired style translation process. The specifics of the EBM are discussed as follows.

The energy-based model, through observing latent code samples, learns to model a distribution that is close to the true data distribution of a target site in latent space, denoted as $\mathbb{P}_\theta(Z_y) \sim \mathbb{P}_{Data}(Y)$. Specifically, we assume that $\mathbb{P}_\theta(Z_y)$ follows a Gibbs distribution (Du and Mordatch, 2019; Xiao et al., 2020), which is defined as $\mathbb{P}_\theta(Z_y) = \frac{1}{Q(\theta)} \exp(-\mathcal{E}_\theta(Z_y))$, where $\mathcal{E}_\theta(Z_y) : \mathbb{R}^D \rightarrow \mathbb{R}$ is a scalar energy function parameterized by θ . This function $\mathcal{E}_\theta(Z_y)$ is trained to produce lower energy values to observed latent code samples within the target latent distribution and higher energy values to other inputs. And $Q(\theta) = \int \exp(-\mathcal{E}_\theta(Z_y)) dZ_y$ is the partition function for probability normalization, which is intractable. One can optimize EBM by maximizing the derivative of negative log-likelihood or equivalently minimizing its inverse, formulated as:

$$\begin{aligned} \mathcal{L}_{EBM} &= -(\frac{\partial}{\partial \theta} - L(\theta)) \\ &= -(\mathbb{E}_{Z_y \sim \mathbb{P}_{Data}}[\frac{\partial}{\partial \theta} \mathcal{E}_\theta(Z_y)] - \mathbb{E}_{\tilde{Z}_y \sim \mathbb{P}_\theta}[\frac{\partial}{\partial \theta} \mathcal{E}_\theta(\tilde{Z}_y)]) \end{aligned} \quad (6)$$

where the first expectation term \mathbb{E}_{Z_y} corresponds to samples Z_y , which are drawn from the actual target data distribution $\mathbb{P}_{Data}(Y)$. On the other hand, the second expectation term $\mathbb{E}_{\tilde{Z}_y}$ corresponds to samples \tilde{Z}_y , which are drawn from the modeled distribution \mathbb{P}_θ . This requires direct sampling from \mathbb{P}_θ , an intractable model distribution. This can be approximated using a Markov chain Monte Carlo (MCMC) sampling method, namely the Stochastic Gradient Langevin Dynamics (SGLD) (Welling and Teh, 2011), an iterative method defined as follows:

$$\tilde{Z}_y^{t+1} = \tilde{Z}_y^t - \frac{\eta^t}{2} \frac{\partial}{\partial \tilde{Z}_y^t} \mathcal{E}_\theta(\tilde{Z}_y^t) + \sqrt{\eta^t} \epsilon^t, \quad \epsilon^t \sim \mathcal{N}(0, I) \quad (7)$$

where $t = [0, \dots, T]$ represents the sampling steps with a step size η and ϵ is a Gaussian noise that is injected to account for data uncertainty and to improve sample convergence (LeCun et al., 2006). The initial \tilde{Z}_y^0 are latent codes sampled from the source site X , denoted as $\tilde{Z}_y^0 = Z_x = E(\mathbf{x})$. The SGLD sampling process involves iteratively updating the initial source latent codes

using negative gradients of the energy function \mathcal{E}_θ . This sampling process can be interpreted as evolving original source latent codes towards a configuration with lower energy, thereby *aligning them more closely with the true target latent distribution*. In contrast to source-to-reference image translation (Liu et al., 2021; Zhu et al., 2017; Choi et al., 2020), EBM effectively traverses the latent space of the entire target domain, allowing a comprehensive consideration for intra-site variations within the target domain. After T sampling steps (via SGLD), we can decode \tilde{Z}_y^T through G to generate a translated MRI, denoted as $\tilde{\mathbf{y}} = G(Z_{x \rightarrow y}) = G(\tilde{Z}_y^T)$.

Considering that the EBM does not differentiate the content code and the style code explicitly during style translation, we further introduce a **latent content loss** into the EBM for regularization. This loss function measures the difference between the translated latent code $Z_{x \rightarrow y}$ and the original source latent code Z_x , which is formulated as:

$$\mathcal{L}_{con} = \mathbb{E}_{Z_x \sim \mathbb{P}_{Data}, Z_{x \rightarrow y} \sim \mathbb{P}_\theta}[\|Z_x - Z_{x \rightarrow y}\|_1] \quad (8)$$

To guarantee the learned translation is bijective and to further avoid mode collapse during unpaired latent style translation, we introduce a **latent cycle-consistency loss**, defined as:

$$\mathcal{L}_{cyc} = \mathbb{E}_{Z_x \sim \mathbb{P}_{Data}}[\|Z_x - \mathbb{P}_\theta^{-1} \circ E \circ G \circ \mathbb{P}_\theta(Z_x)\|_1] \quad (9)$$

where \mathbb{P}_θ^{-1} represents the same EBM as \mathbb{P}_θ , but it operates with an inverse SGLD sampling process. This means that it will update the latent code using positive gradients of the energy function, in contrast to the negative gradients used by \mathbb{P}_θ .

With the integration of Eqs. (6), (8)-(9), the full objective function of SST can be written as:

$$\mathcal{L}(\theta) = \mathcal{L}_{EBM} + \alpha \mathcal{L}_{con} + \beta \mathcal{L}_{cyc} \quad (10)$$

where α and β serve as hyperparameters that determine the relative contributions of the three terms in the equation. By disentangling image generation via SIG and style translation via SST in the low-dimensional latent space, it is expected to achieve efficient and generalizable MRI harmonization.

3.2.4. Site-Specific MRI Synthesis (SMS)

In the proposed SST module, we can substitute the original source MRI and encoder E with a random Gaus-

sian noise z and the mapping network F to perform *site-specific MRI synthesis*. In this case, as the network F has already been trained in the SIG to generate latent codes resembling brain MRIs, no further fine-tuning is required. The EBM will then translate these randomly generated latent codes into the target style for image synthesis. Unlike many MRI synthesis models that only generate MRI with random anatomical structures and styles, our framework can synthesize MRIs with a consistent intensity distribution that matches a given image domain, this can be effectively used as a data augmentation method to pre-train models that require large number of MRI samples without introducing non-biological variations caused by difference in imaging style.

3.2.5. Implementation

The implementation of SIG incorporates similar settings as outlined in (Pidhorskyi et al., 2020), with structural modifications made to accommodate our specific datasets and tasks. Specifically, both the mapping function F and the latent discriminator D are implemented using multi-layer perceptions (MLPs). The former consists of eight layers, while the latter is composed of three layers. Two networks E and G in the latent autoencoder are composed of seven encoding/decoding blocks. Each of these blocks incorporates an increasing number of filters, ranging from 64 to 256 filters. All latent codes have a dimension of 512 in the experiments. We train the SIG module using an Adam (Kingma and Ba, 2014) optimizer in an *unsupervised training* scheme. Compared to GANs (Zhu et al., 2017; Choi et al., 2020), SIG’s training cost is lower due to two factors: (1) most of its losses are evaluated in low-dimensional latent space, and (2) no additional cost for cycle-consistency constraints in image space. Following the SIG training, we can directly use the latent autoencoder in SST training, during which E and G are not updated.

The training of the SST is *efficient in both training time and computational cost* due to four factors. (1) The autoencoder E and G do not require additional training, even when deployed on previously unseen data. (2) The style translation process, facilitated by EBM, operates in a low-dimensional latent space with a dimension of 512, which is considerably smaller than the image space. (3) The energy function \mathcal{E}_θ in EBM is designed to be light-weight, also implemented as an MLP with 2 layers, each having

a dimension of 2,048. (4) The SST can be trained with a small sample size for each target site (*i.e.*, ~ 120 slices in our experiments). In this way, our DLEST can achieve efficient imaging style translation and generalizable MRI generation through the disentanglement scheme.

4. Experiments

4.1. Experimental Settings

4.1.1. Competing Methods

We first compare DLEST with two non-learning methods, including (1) histogram matching (**HM**) (Shinohara et al., 2014) with multiple experiments with randomly selected reference MRI from the target dataset, and (2) Spectrum Swapping-based Image-level Harmonization (**SSIMH**), which replaces certain low-frequency region of the source MRI with the corresponding low-frequency spectrum of the reference MRI, with a default swapping threshold 3. We use the DomainATM toolbox (Guan and Liu, 2023) to carry out two non-learning methods. We also compare DLEST against the following state-of-the-art (SOTA) methods for unpaired image-level harmonization.

(1) **CycleGAN** (Zhu et al., 2017) is initially introduced for natural image-to-image translation. It enhances the capabilities of traditional GANs by integrating an important cycle-consistency constraint. This additional constraint enables the unpaired mapping from a source domain to a target domain. The CycleGAN has been utilized in several MRI harmonization studies (Modanwal et al., 2020; Chang et al., 2022) and has become the foundational structure of many subsequent image-level harmonization methods.

(2) **StarGAN** (Choi et al., 2020) is initially introduced for multi-domain natural image synthesis task. Then, it was employed for MRI harmonization (Liu et al., 2021). Building upon CycleGAN, the StarGAN method learns a separate latent style code for each target image and injects this code into the source image via instance normalization.

(3) **ImUnity** (Cackowski et al., 2023) is designed specifically for MRI harmonization. It employs a self-supervised variational autoencoder model, coupled with a confusion module for site/scanner-bias unlearning. In addition, it includes an optional biological preservation

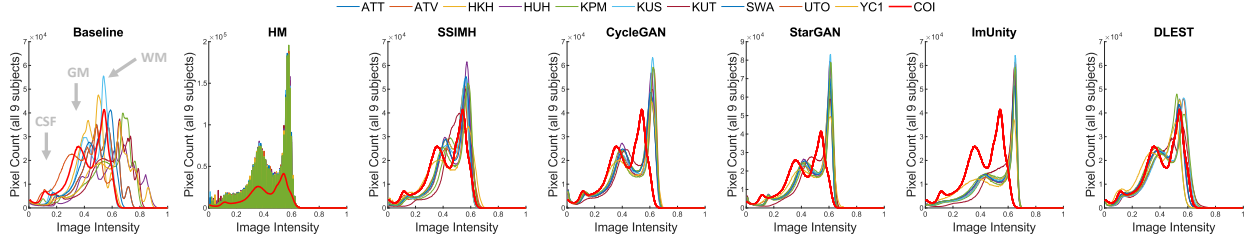


Figure 2: Histogram comparison of 10 source sites and a target site (COI) from the SRPBS dataset. The first plot shows pre-harmonization histograms, while the subsequent plots depict post-harmonization histograms by each competing method and our method DLEST, respectively. WM: white matter; GM: gray matter; CSF: cerebrospinal fluid.

module to preserve clinical information, such as disease labels or diagnostic scores. In this work, we use the default form of ImUnity without this optional module, since the two datasets only consist of healthy control subjects.

In all three deep learning methods mentioned above, we typically adhere to the default setting of each competing method and make a dedicated effort to ensure other training hyperparameters align closely with the proposed DLEST framework. In DLEST, the two hyperparameters α and β in Eq. 10 are empirically set as 100 and 10, respectively. For a fair comparison, we standardize the input size to be 256×256 and set the latent dimension to 512, mirroring the specifications of the proposed DLEST. To train deep learning models (*i.e.*, CycleGAN, StarGAN, ImUnity, and our DLEST), we use the OpenBHB dataset, due to its relatively larger sample size and abundant sites/settings. Following (Dufumier et al., 2022), 3,227 training scans and 757 validation scans from 58 sites/settings are used with manual inspection and quality control.

4.1.2. Evaluation Tasks

Four tasks are performed in the experiments: (1) histogram and clustering comparison, (2) site classification, (3) brain tissue segmentation, and (4) site-specific MRI synthesis. The SRPBS is used in Tasks 1, 3, and 4 because traveling subjects are available. The OpenBHB is used in Task 2 and Task 4.

4.2. Experimental Results

4.2.1. Task 1: Histogram & Clustering Comparison

We first qualitatively evaluate our DLEST by comparing histogram and clustering of MRIs before harmonization (Baseline) and post-harmonization produced by each

competing method in Fig. 2. The validation is performed on SRPBS since each subject has ground-truth scans on multiple acquisition sites. We treat the COI as the target domain due to its least intra-site variation, and harmonize the rest 10 sites/settings to the COI.

As observed in Fig. 2, before MRI harmonization (baseline), each site initially exhibits unique intensity distributions. Particularly, three prominent intensity peaks, corresponding to WM, GM, and CSF, are not aligned with the target domain. After harmonization, our DLEST framework demonstrates superior performance in aligning the histogram of the ten source sites with the target COI, particularly excelling in aligning the three main peaks. But the three SOTA deep learning methods (*i.e.*, CycleGAN, StarGAN, and ImUnity) cannot well align source peaks with the target ones, despite showing good peak alignment across the 10 source sites. Our success may be attributed to the model’s ability to learn the latent data distribution of the entire target domain via EBM, while the three deep learning methods do not effectively account for intra-site variation within the target domain. On the other hand, the two non-learning methods cannot produce good performance. For example, the HM method, despite achieving reasonable peak alignment with the target, exhibits a non-smooth artifact in the post-harmonization histogram. This could be due to the significant intensity disparity between the source MRIs and the target/reference MRI (Li et al., 2021), caused by potential site effects.

For MRI clustering, we first employ a VGG network (Simonyan and Zisserman, 2014) to extract image features of the original MRIs and harmonized ones (via DLEST). Subsequently, we apply principle component analysis (with 20 principal components) to reduce the di-

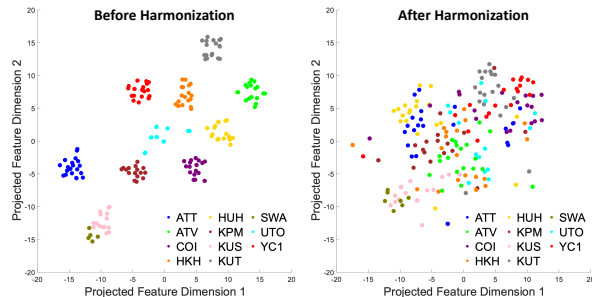


Figure 3: Clustering of 11 sites across 9 subjects from SRPBS, (left) before and (right) after harmonization by DLEST.

mensionality of the extracted image features, and then utilize the t-SNE (Van der Maaten and Hinton, 2008) to reduce the dimensionality of these features and project them into a 2D space. Finally, we apply K-Means clustering algorithm to these features in this 2D space. The results in Fig. 3 show that image features are initially clustered into 11 distinct groups. After harmonization by DLEST, these clusters become less distinguishable, implying that our method effectively eliminates site-related variations in harmonized MRIs.

4.2.2. Task 2: Site Classification

In this task, we conduct a quantitative evaluation to determine the effectiveness of a harmonization method in eliminating site-related, non-biological variations. We begin by selecting a site (ID: 17) from the OpenBHB dataset with minimal intra-site variation as our target domain. We then harmonize MRIs from the rest 57 source sites to this target domain using each method. Following this, we train a site classifier on the OpenBHB training set (with 3,227 MRIs) and validate it on the validation set (with 757 MRIs). The site classifier is implemented based on the ResNet18 (He et al., 2016) architecture. Its performance on raw MRI data is recorded as the Baseline. Five metrics are used: balanced accuracy (BACC), accuracy (ACC), area under the ROC curve (AUC), F1 score (F1), and sensitivity (SEN). The results of site classification are reported in Table 1, where a lower value signifies a method’s better capability to eliminate site-related variations, thereby making it challenging for the site classifier to learn site-related features that could differentiate each site.

As indicated in Table 1, our DLEST method consis-

Table 1: Multi-class (58 categories) site classification results on OpenBHB, where ‘*’ denotes that the difference between a specific competing method and DLEST is statistically significant ($p < 0.05$ via paired t -test).

Method	BACC↓	ACC↓	AUC↓	F1↓	SEN↓
Baseline*	0.676±0.137	0.722±0.147	0.979±0.022	0.713±0.146	0.722±0.147
HM*	0.619±0.133	0.696±0.137	0.981±0.019	0.685±0.129	0.696±0.137
SSIMH*	0.673±0.083	0.659±0.076	0.983±0.008	0.656±0.079	0.659±0.076
CycleGAN*	0.588±0.081	0.660±0.088	0.974±0.007	0.645±0.088	0.660±0.088
StarGAN*	0.489±0.201	0.562±0.223	0.951±0.047	0.543±0.215	0.562±0.223
ImUnity*	0.569±0.074	0.658±0.066	0.978±0.008	0.636±0.066	0.658±0.066
DLEST (Ours)	0.336±0.057	0.483±0.065	0.938±0.020	0.474±0.069	0.483±0.065

tently surpasses the five competing methods by a substantial margin. For instance, after the data is harmonized by DLEST, there is a decrease in BACC by 0.340 compared to the Baseline, and a decrease of 0.153 when compared to the second-best StarGAN method. When compared with the three SOTA methods (*i.e.*, CycleGAN, StarGAN, and ImUnity), our method consistently yields superior results across five metrics. This result is consistent with the qualitative result in Task 1 (see Fig. 2).

Several factors may contribute to the significant performance difference between our DLEST and the three SOTA methods. Unlike CycleGAN, which relies solely on adversarial learning between discriminators and the generators in image space to generate images resembling the target, our DLEST achieves style translation by directly manipulating the latent code of an image via EBM. This direct manipulation of latent code allows our DLEST to have fine-grained control over style translation. Furthermore, DLEST captures the underlying data distribution of the entire target site when translating an image to the target style. In contrast, StarGAN treats each target image as a unique “domain” with its own style and depends on a single reference image during style translation. Similarly, while ImUnity learns an unbiased latent representation devoid of site information, it still necessitates a single reference image for “contrast correction”. These quantitative results further suggest the superiority of DLEST in capturing the latent distribution of the target domain for effective style translation.

4.2.3. Task 3: Brain Tissue Segmentation

This experiment is designed to assess the effectiveness of the DLEST on a downstream brain tissue (*i.e.*, WM, GM, and CSF) segmentation task. We begin by selecting a source site (*i.e.*, HUH) and a target site (*i.e.*, COI) within the SRPBS dataset and harmonize the source MRIs to the

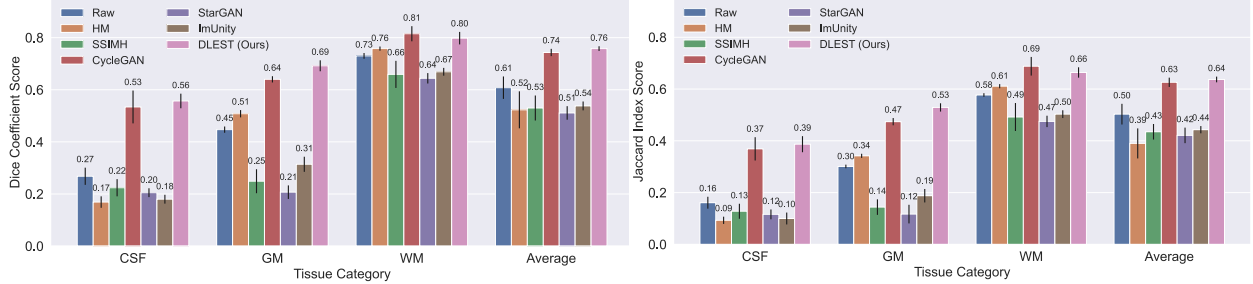


Figure 4: Segmentation results of CSF, GM, and WM on SRPBS in terms of (left) Dice coefficient and (right) Jaccard index. Each U-Net is trained on the target site COI and validated the source site HUH from SRPBS.

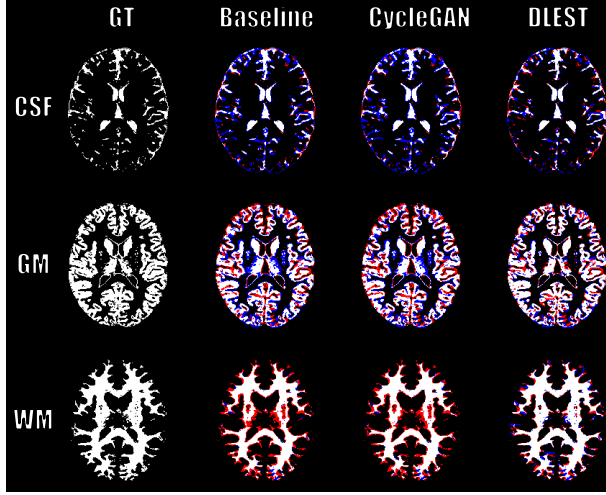


Figure 5: Sample U-Net segmentation of brain tissues (CSF, GM, WM) using unharmonized data (Baseline) and data harmonized by CycleGAN (top competing method) and DLEST (ours). White pixels denote the correct segmentation, red pixels denote under-segmentation, and blue pixels denote over-segmentation.

target domain using DLEST and each competing method. Following this, a U-Net (Ronneberger et al., 2015) segmentation model is trained on MRIs from the target site (COI) and directly validated on the source site (HUH). As our primary objective is to assess the impact of each harmonization method on tissue segmentation, the quality of the ground-truth segmentation is not our main concern. We thus utilize the segmentation masks obtained using the FAST pipeline in FSL as our ground truth to provide a fair basis for comparing each method. For each harmonization method, the U-Net is trained for 100 epochs, with the mean and standard deviation of the validation Dice co-

efficient and the Jaccard index reported for the final 40 epochs.

Quantitatively, as shown in Fig. 4, our DLEST method consistently surpasses all non-learning methods (*i.e.*, HM and SSIMH), suggesting that the latent space style translation is more effective than merely aligning the global intensity distribution. Compared with three SOTA methods, our DLEST consistently delivers superior performance in terms of average segmentation results and specifically in the segmentation of CSF and GM. While CycleGAN slightly outperforms DLEST in WM segmentation, our DLEST exhibits a significantly lower standard deviation. This indicates that the DLEST produces a more stable performance compared to CycleGAN.

In addition, Fig. 5 presents the comparative visualization of brain tissue segmentation results. The first column displays the ground truth (GT) segmentation maps, derived from FSL. The subsequent columns represent the results of three identically structured U-Nets, all trained on the target domain (*i.e.*, COI) MRIs. In particular, the **Baseline** column shows validation results on unharmonized source domain (*i.e.*, HUH) MRIs. The **CycleGAN** column presents the validation results on the source domain MRIs, post-harmonization to the target domain using the top competing method (*i.e.*, CycleGAN). Similarly, the **DLEST** column depicts the validation results on source domain MRIs harmonized using our method. In this figure, the segmentation map uses white pixels to indicate accurate segmentation, while red and blue pixels represent under-segmentation and over-segmentation, respectively. Notably, the U-Net trained on DLEST-harmonized data demonstrated significant improvements, particularly in reducing under-segmentation of white mat-

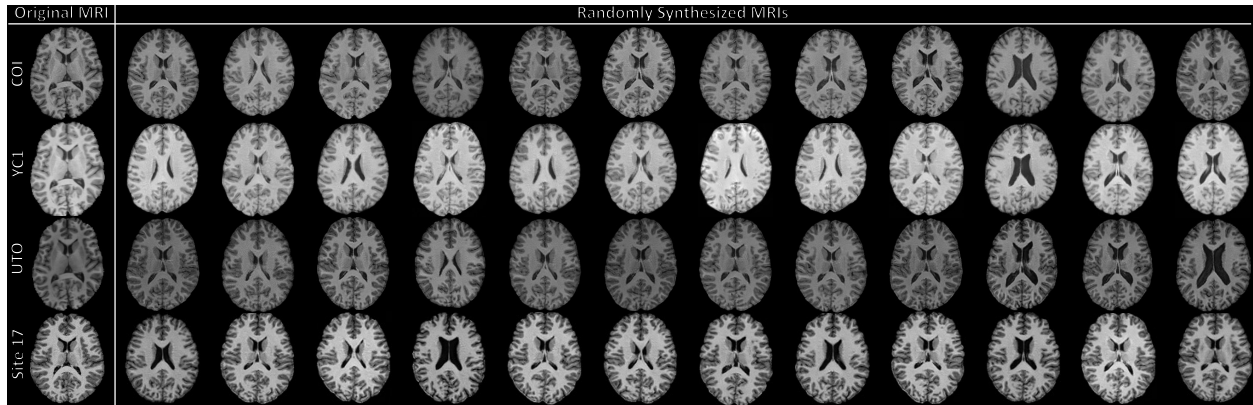


Figure 6: Synthesized MRI with site-specific styles of 3 sites from SRPBS (top 3 rows) and 1 site from OpenBHB (bottom row). The synthetic MRIs have diverse anatomical structures with consistent image styles that match the reference MRI from a specific site.

ter near tissue boundaries and over-segmentation of gray matter near the thalamus region.

4.2.4. Task 4: MRI Synthesis

This task aims to demonstrate our framework’s ability to synthesize brain MRIs with site-specific styles. We select three sites from the SRPBS dataset and one site from the OpenBHB dataset for illustration. We evaluate the quality of the synthesis qualitatively via sample visualization and quantitatively through the structural similarity index measurement (SSIM) (Wang et al., 2004), peak signal-to-noise ratio (PSNR), and root mean square error (RMSE). As shown in Fig. 6, our DLEST is able to synthesize new brain MRIs with diverse brain shapes and anatomical structures while preserving the site-specific styles that match the given reference MRI scans. This latent space MRI synthesis is cost-efficient and helpful in training non-disease specific learning models that require large quantities of MRI samples while the actual MRI data is limited, such as brain segmentation models.

For quantitative evaluation, we report the mean and the standard deviation of image-level metrics for synthesized MRIs at each site in Table 2. Metrics under the **Original** category are derived from comparisons between each original image and every other original image within the same site. The **Synthesized** category metrics are obtained by comparing each synthesized image with all original images from the same site. The marginal differences observed across all metrics between Original and Synthesized image pairs suggest that our DLEST framework can

Table 2: Quantitative result of the image-level metrics. Original denotes mean and standard deviation between every pair of original images; and Synthesized denotes mean and standard deviation between every pair of original and synthesized images.

Site ID	MRI	SSIM \uparrow	PSNR \uparrow	RMSE \downarrow
COI	Original	0.829 \pm 0.025	21.590 \pm 1.718	0.085 \pm 0.013
	Synthesized	0.828 \pm 0.017	20.740 \pm 1.485	0.093 \pm 0.016
YC1	Original	0.838 \pm 0.028	19.883 \pm 2.236	0.104 \pm 0.022
	Synthesized	0.830 \pm 0.019	19.723 \pm 1.456	0.105 \pm 0.018
UTO	Original	0.840 \pm 0.031	21.387 \pm 2.323	0.088 \pm 0.018
	Synthesized	0.833 \pm 0.017	21.405 \pm 1.372	0.086 \pm 0.014
Site 17	Original	0.800 \pm 0.025	18.936 \pm 1.541	0.115 \pm 0.016
	Synthesized	0.788 \pm 0.015	18.421 \pm 0.951	0.121 \pm 0.013

effectively generate synthetic MRIs that maintain consistent styles and quality comparable to the original images.

5. Discussion

5.1. Ablation Study

We investigate three downgraded variants of the proposed DLEST framework, namely (1) **DLEST-PIX**, which excludes pixel-wise loss in Eq. (5) during the SIG module training, (2) **DLEST-CON**, which omits the latent content loss in Eq. (10), and (3) **DLEST-CYC**, which does not incorporate the latent cycle-consistency loss in Eq. (10) when training the SST module for style translation. We train DLEST and its three variants on the SRPBS traveling subject dataset and evaluate their harmonization results using two image quality metrics: SSIM

and PSNR. As indicated in Fig. 7 (a), while all ablations negatively impact the result, DLEST-PIX particularly yields the worst results, compared with its two counterparts. This implies that the pixel-wise, latent content and cycle-consistency losses are necessary to ensure a satisfying harmonization outcome, and especially, the pixel-wise loss plays a crucial role in preserving image content in DLEST.

5.2. Influence of Hyperparameters

We conduct several rounds of hyperparameter tuning to examine the influence of hyperparameters α and β in Eq. (10) on the harmonization effect. This involved varying one parameter while maintaining the other constant. The results in Fig. 7 (b)-(c) suggest that the model’s performance improves when the latent content loss has more weight (*i.e.*, with a larger α) in the overall loss function. Additionally, the performance of DLEST appears to be less sensitive to variations in β .

5.3. Influence of Content Loss

Following (Zhao and Chen, 2021), our implementation uses a latent content loss in Eq. (8) to minimize the change of anatomical structure during style translation. This implicit regularization in latent space may cause slight alterations of anatomical details. To this end, we compare our method with its variant **DLEST+CS** that utilizes a separate style and content loss (Gatys et al., 2016) to *explicitly enforce content preservation* while allowing the style to be translated freely. In DLEST+CS, a pre-trained VGG19 (Simonyan and Zisserman, 2014) is used to extract feature maps of given MRI slices. The *content loss* is calculated as the l_2 distance between the extracted feature maps of original MRI and the translated MRI in specific layers. The *style loss* is computed as the weighted average of l_2 distance between Gram matrices (Gatys et al., 2016) of the target and translated MRIs in each layer. The Gram matrix is a correlation matrix between each feature map, where each entry \mathcal{G}_{ij} is the inner product of vectorized feature maps i and j . By including feature correlations of multiple layers, we obtain a multi-scale representation of the input image, which captures its texture characteristics without content information (Gatys et al., 2016). As shown in Fig. 7 (a), compared with DLEST, its variant DLEST+CS achieves slight improvement in terms

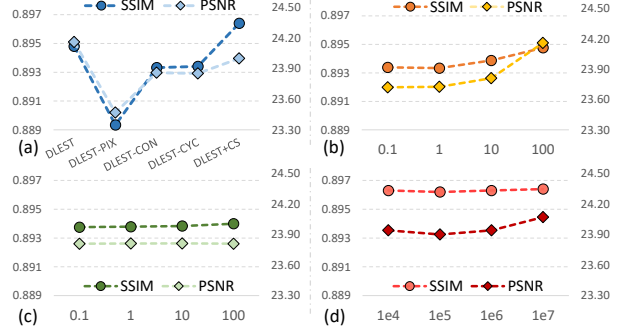


Figure 7: Results of (a) DLEST variants, DLEST with different values of (b) α and (c) β , and (d) different ratios of style/content loss.

of SSIM, implying enhanced content preservation. However, the improvement of DLEST+CS is accompanied by a significant increase in computation cost, as the calculation of style and content loss in ambient space, which requires decoding latent codes into image slices within EBM.

5.4. Comparison with Feature-Level Harmonization

Although the primary motivation behind proposing an image-level harmonization approach is its adaptability to a variety of downstream tasks, it remains crucial to compare our DLEST framework with the prevalent feature-level harmonization method, ComBat (Johnson et al., 2007). This comparison generally follows the evaluation scheme outlined in the OpenBHB Challenge (Dufumier et al., 2022) to ensure a fair assessment of both methodologies. Specifically, we employ the official Python implementation of ComBat (Fortin, 2023; Johnson et al., 2007) to harmonize a collection of seven pre-extracted MRI features. These features include cortical thickness (along with standard deviation), GM volume, surface area, integrated mean (and Gaussian) curvature, and intrinsic curvature index for each subject in the training set. Subsequently, we train a linear logistic regression model (Pedregosa et al., 2011) on these harmonized features and evaluate its multi-class site classification performance on the validation set. Similarly, for the image-level approach, we utilize a VGG19 feature extractor (with weights frozen) to directly extract image features from the harmonized MRIs, and train a comparable linear logistic regression model for site classification. We also compare two baselines, named **Baseline-F** and **Baseline-I**

Table 3: Site classification result of linear model where ‘*’ denotes the difference between a specific method and DLEST is statistically significant ($p < 0.05$ via paired t-test).

Method	BACC↓	ACC↓	F1↓
Baseline-F	$0.703 \pm 0.019^*$	$0.762 \pm 0.008^*$	$0.739 \pm 0.020^*$
Baseline-I	$0.311 \pm 0.087^*$	$0.505 \pm 0.086^*$	$0.451 \pm 0.083^*$
ComBat	$0.586 \pm 0.158^*$	$0.566 \pm 0.213^*$	$0.525 \pm 0.230^*$
CycleGAN	0.134 ± 0.029	0.392 ± 0.060	$0.303 \pm 0.046^*$
StarGAN	$0.178 \pm 0.053^*$	0.430 ± 0.112	$0.352 \pm 0.088^*$
ImUnity	$0.196 \pm 0.043^*$	0.406 ± 0.107	$0.350 \pm 0.080^*$
DLEST (Ours)	0.130 ± 0.010	0.407 ± 0.013	0.321 ± 0.010

that correspond to the original MRI features and images, respectively. The accuracy and balanced accuracy, and F1 score are reported, with lower performance indicating more effective harmonization. As shown in Table 3, both the original MRI scans and extracted MRI features are characterized by a significant amount of site-related variations. ComBat performs better than Baseline-F, indicating its efficacy in feature harmonization. However, it only addresses the site effect on the pre-extracted features, rather than the entire image level, limiting its utility in broader applications. In contrast, our method successfully eliminates the majority of the site-related variations, resulting in the lowest BACC for the linear model.

5.5. Computational Cost Evaluation

To quantitatively assess the enhancements in computational and time efficiency, we compare our DLEST framework with three GAN-based SOTA methods across several metrics. These include the number of trainable parameters, total floating point operations (FLOPs) per forward pass, training time to convergence on the OpenBHB training dataset, testing time on the SRPBS dataset, and the necessity for retraining when applied to an unseen dataset. As demonstrated in Table 4, our model, encompassing both the SIG and SST modules, contains the fewest parameters, requires significantly fewer FLOPs per forward pass, and generally requires less training time. Furthermore, in comparison to ImUnity, which can also generalize to unseen data without retraining, our DLEST framework requires less time to fine-tune solely the SST module. These results collectively suggest that our DLEST can achieve highly efficient and generalizable MRI harmonization.

Table 4: Time and computation cost. For DLEST, $a + b$ denotes the number for SIG + SST. Test time is the cost of generalizing on an unseen dataset. M: Million; GMac: Giga multiply-accumulate operations; H: Hour.

Method	#Parameters (M)	FLOPs (GMac)	Training Time (H)	Test Time (H)	Need Re-training
CycleGAN	28.3	1794.1	29.1	8.0	<i>Yes</i>
StyleGAN	161.3	4865.3	53.8	9.1	<i>Yes</i>
ImUnity	671.0	246.2	25.3	1.5	<i>No</i>
DLEST (Ours)	21.7+5.3	2.1+0.3	20.0+0.4	0.4	<i>No</i>

5.6. Limitations and Future Work

While extensive experiments demonstrate that the proposed DLEST is competitive over SOTA methods, it is important to acknowledge some limitations. *First*, our current implementation focuses on 2D-level MRI slices, potentially overlooking volumetric variations, and can only synthesize discontinued MRI slices instead of the whole volume. One possible solution is to extend our implementation to 2.5D, incorporating a conditioning mechanism in the autoencoder to generate MRI slices by conditioning on adjacent slices (Peng et al., 2022). *Second*, our current autoencoder employs a one-dimensional latent code to achieve the most efficient encoding and style translation. However, the aggressive 1D encoding discards some inherent spatial structures of the original image, leading to some minor loss of anatomical structures during reconstruction. It is interesting to employ 2D latent encoding (Rombach et al., 2022) with a relatively mild compression rate to better preserve anatomical structures of input MRIs, which will be one of our future works. *In addition*, our current work only uses latent information from images, without considering biological features, such as gender, age, and relevant clinical diagnostic scores. As our further work, we plan to incorporate biological variables as condition to improve fidelity of generated images.

6. Conclusion

This paper proposes a novel unpaired image-level harmonization framework for multi-site MRI data. By disentangling site-invariant image generation and site-specific style translation, our model can generalize on new sites without any retraining on original data. The style translation in latent space efficiently harmonizes multiple source

sites to the target site. Moreover, the model can synthesize diverse MRIs in a site-specific style without additional training. Quantitative and qualitative evaluations suggest that our DLEST outperforms several state-of-the-art harmonization methods. Additionally, our framework can be employed as a pre-processing step in downstream studies, such as mitigating site effects in multi-site MRIs and synthesizing MRIs to train general models.

References

- Albayram, M.S., Smith, G., Tufan, F., Tuna, I.S., Bostancıklouglu, M., Zile, M., Albayram, O., 2022. Non-invasive MR imaging of human brain lymphatic networks with connections to cervical lymph nodes. *Nature Communications* 13, 203.
- An, L., Chen, J., Chen, P., Zhang, C., He, T., Chen, C., Zhou, J.H., Yeo, B.T., 2022. Goal-specific brain MRI harmonization. *NeuroImage* 263, 119570.
- Cackowski, S., Barbier, E.L., Dojat, M., Christen, T., 2023. Imunity: A generalizable VAE-GAN solution for multicenter MR image harmonization. *Medical Image Analysis* 88, 102799.
- Chang, X., Cai, X., Dan, Y., Song, Y., Lu, Q., Yang, G., Nie, S., 2022. Self-supervised learning for multi-center magnetic resonance imaging harmonization without traveling phantoms. *Physics in Medicine & Biology* 67, 145004.
- Choi, Y., Uh, Y., Yoo, J., Ha, J.W., 2020. Stargan v2: Diverse image synthesis for multiple domains, in: *IEEE/CVF Conference on Computer Vision and Pattern Recognition*, pp. 8188–8197.
- Deoni, S.C., Williams, S.C., Jezzard, P., Suckling, J., Murphy, D.G., Jones, D.K., 2008. Standardized structural magnetic resonance imaging in multicentre studies using quantitative T1 and T2 imaging at 1.5 T. *NeuroImage* 40, 662–671.
- Dewey, B.E., Zuo, L., Carass, A., He, Y., Liu, Y., Mowry, E.M., Newsome, S., Oh, J., Calabresi, P.A., Prince, J.L., 2020. A disentangled latent space for cross-site MRI harmonization, in: *Medical Image Computing and Computer-Assisted Intervention*, Springer. pp. 720–729.
- Du, Y., Mordatch, I., 2019. Implicit generation and modeling with energy based models. *Advances in Neural Information Processing Systems* 32.
- Dufumier, B., Grigis, A., Victor, J., Ambroise, C., Frouin, V., Duchesnay, E., 2022. OpenBHB: A large-scale multi-site brain MRI data-set for age prediction and debiasing. *NeuroImage* 263, 119637.
- Evans, P., Sokolska, M., Alves, A., Harrison, I., Ohene, Y., Nahavandi, P., Ismail, O., Miranda, E., Lythgoe, M., Thomas, D., et al., 2020. Non-invasive MRI of blood–cerebrospinal fluid barrier function. *Nature Communications* 11, 2081.
- Fortin, J.P., 2023. NeuroCombat: Python implementation of the NeuroCombat harmonization method. <https://github.com/Jfortin1/neuroCombat>.
- Gatys, L.A., Ecker, A.S., Bethge, M., 2016. Image style transfer using convolutional neural networks, in: *IEEE Conference on Computer Vision and Pattern Recognition*, pp. 2414–2423.
- Glocker, B., Robinson, R., Castro, D.C., Dou, Q., Konukoglu, E., 2019. Machine learning with multi-site imaging data: An empirical study on the impact of scanner effects. *arXiv preprint arXiv:1910.04597*.
- Guan, H., Liu, M., 2023. DomainATM: Domain adaptation toolbox for medical data analysis. *NeuroImage* 268, 119863.
- Gulrajani, I., Ahmed, F., Arjovsky, M., Dumoulin, V., Courville, A.C., 2017. Improved training of Wasserstein GANs. *Advances in Neural Information Processing Systems* 30.
- He, K., Zhang, X., Ren, S., Sun, J., 2016. Deep residual learning for image recognition, in: *IEEE Conference on Computer Vision and Pattern Recognition*, pp. 770–778.
- Helmer, K.G., Chou, M.C., Preciado, R., Gimi, B., Rollins, N., Song, A., Turner, J., Mori, S., 2016. Multi-site study of diffusion metric variability: Characterizing the effects of site, vendor, field strength, and echo time using the histogram distance, in: *Biomedical Applications in Molecular, Structural, and Functional Imaging*, pp. 363–373.

- Jack Jr, C.R., Bernstein, M.A., Fox, N.C., Thompson, P., Alexander, G., Harvey, D., Borowski, B., Britson, P.J., L. Whitwell, J., Ward, C., et al., 2008. The Alzheimer’s disease neuroimaging initiative (ADNI): MRI methods. *Journal of Magnetic Resonance Imaging* 27, 685–691.
- Johnson, W.E., Li, C., Rabinovic, A., 2007. Adjusting batch effects in microarray expression data using empirical Bayes methods. *Biostatistics* 8, 118–127.
- Kingma, D.P., Ba, J., 2014. Adam: A method for stochastic optimization. *arXiv preprint arXiv:1412.6980*.
- Kingma, D.P., Welling, M., 2013. Auto-encoding variational Bayes. *arXiv preprint arXiv:1312.6114*.
- LeCun, Y., Chopra, S., Hadsell, R., Ranzato, M., Huang, F., 2006. A tutorial on energy-based learning. *Predicting Structured Data* 1.
- Li, Y., Ammari, S., Balleyguier, C., Lassau, N., Chouzenoux, E., 2021. Impact of preprocessing and harmonization methods on the removal of scanner effects in brain MRI radiomic features. *Cancers* 13, 3000.
- Liu, M., Maiti, P., Thomopoulos, S., Zhu, A., Chai, Y., Kim, H., Jahanshad, N., 2021. Style transfer using generative adversarial networks for multi-site MRI harmonization, in: *Medical Image Computing and Computer Assisted Intervention, Part III* 24, Springer. pp. 313–322.
- Van der Maaten, L., Hinton, G., 2008. Visualizing data using t-SNE. *Journal of Machine Learning Research* 9.
- Modanwal, G., Vellal, A., Buda, M., Mazurowski, M.A., 2020. MRI image harmonization using cycle-consistent generative adversarial network, in: *Computer-Aided Diagnosis, SPIE*. pp. 259–264.
- Ng, A., Jordan, M., 2001. On discriminative vs. generative classifiers: A comparison of logistic regression and naive bayes. *Advances in Neural Information Processing Systems* 14.
- Pang, B., Han, T., Nijkamp, E., Zhu, S.C., Wu, Y.N., 2020. Learning latent space energy-based prior model. *Advances in Neural Information Processing Systems* 33, 21994–22008.
- Pedregosa, F., Varoquaux, G., Gramfort, A., Michel, V., Thirion, B., Grisel, O., Blondel, M., Prettenhofer, P., Weiss, R., Dubourg, V., et al., 2011. Scikit-learn: Machine learning in Python. *the Journal of Machine Learning Research* 12, 2825–2830.
- Peng, W., Adeli, E., Zhao, Q., Pohl, K.M., 2022. Generating realistic 3D brain MRIs using a conditional diffusion probabilistic model. *arXiv preprint arXiv:2212.08034*.
- Pidhorskyi, S., Adjero, D.A., Doretto, G., 2020. Adversarial latent autoencoders, in: *IEEE/CVF Conference on Computer Vision and Pattern Recognition*, pp. 14104–14113.
- Pomponio, R., Erus, G., Habes, M., Doshi, J., Srinivasan, D., Mamourian, E., Bashyam, V., Nasrallah, I.M., Satterthwaite, T.D., Fan, Y., et al., 2020. Harmonization of large MRI datasets for the analysis of brain imaging patterns throughout the lifespan. *NeuroImage* 208, 116450.
- Rombach, R., Blattmann, A., Lorenz, D., Esser, P., Ommer, B., 2022. High-resolution image synthesis with latent diffusion models, in: *Computer Vision and Pattern Recognition*, pp. 10684–10695.
- Ronneberger, O., Fischer, P., Brox, T., 2015. U-Net: Convolutional networks for biomedical image segmentation, in: *Medical Image Computing and Computer-Assisted Intervention, Part III* 18, pp. 234–241.
- Schnack, H.G., van Haren, N.E., Brouwer, R.M., van Baal, G.C.M., Picchioni, M., Weisbrod, M., Sauer, H., Cannon, T.D., Huttunen, M., Lepage, C., et al., 2010. Mapping reliability in multicenter MRI: Voxel-based morphometry and cortical thickness. *Human Brain Mapping* 31, 1967–1982.
- Shinohara, R.T., Sweeney, E.M., Goldsmith, J., Shiee, N., Mateen, F.J., Calabresi, P.A., Jarso, S., Pham, D.L., Reich, D.S., Crainiceanu, C.M., et al., 2014. Statistical normalization techniques for magnetic resonance imaging. *NeuroImage: Clinical* 6, 9–19.
- Simonyan, K., Zisserman, A., 2014. Very deep convolutional networks for large-scale image recognition. *arXiv preprint arXiv:1409.1556*.

- Smith, S.M., Jenkinson, M., Woolrich, M.W., Beckmann, C.F., Behrens, T.E., Johansen-Berg, H., Bannister, P.R., De Luca, M., Drobnjak, I., Flitney, D.E., et al., 2004. Advances in functional and structural MR image analysis and implementation as FSL. *NeuroImage* 23.
- Styner, M.A., Charles, H.C., Park, J., Gerig, G., 2002. Multisite validation of image analysis methods: Assessing intra-and intersite variability, in: *Image Processing*, pp. 278–286.
- Sun, Y., Gao, K., Wu, Z., Li, G., Zong, X., Lei, Z., Wei, Y., Ma, J., Yang, X., Feng, X., et al., 2021. Multi-site infant brain segmentation algorithms: the iSeg-2019 challenge. *IEEE Transactions on Medical Imaging* 40, 1363–1376.
- Tanaka, S., Yamashita, A., Yahata, N., Itahashi, T., Lisi, G., Yamada, T., Ichikawa, N., Takamura, M., Yoshihara, Y., Kunimatsu, A., Okada, N., Hashimoto, R., Okada, G., Sakai, Y., Morimoto, J., Narumoto, J., Shimada, Y., Mano, H., Yoshida, W., Imamizu, H., 2021. A multi-site, multi-disorder resting-state magnetic resonance image database. *Scientific Data* 8, 227. doi:10.1038/s41597-021-01004-8.
- Tofts, P., Collins, D., 2011. Multicentre imaging measurements for oncology and in the brain. *The British Journal of Radiology* 84, S213–S226.
- Varela, M., Morgan, R., Theron, A., Dillon-Murphy, D., Chubb, H., Whitaker, J., Henningsson, M., Aljabar, P., Schaeffter, T., Kolbitsch, C., et al., 2017. Novel MRI technique enables non-invasive measurement of atrial wall thickness. *IEEE Transactions on Medical Imaging* 36, 1607–1614.
- Wachinger, C., Rieckmann, A., Pölsterl, S., 2021. Detect and correct bias in multi-site neuroimaging datasets. *Medical Image Analysis* 67, 101879.
- Wang, Z., Bovik, A.C., Sheikh, H.R., Simoncelli, E.P., 2004. Image quality assessment: From error visibility to structural similarity. *IEEE Transactions on Image Processing* 13, 600–612.
- Welling, M., Teh, Y.W., 2011. Bayesian learning via stochastic gradient langevin dynamics, in: *International Conference on Machine Learning*, pp. 681–688.
- Wu, M., Zhang, L., Yap, P.T., Lin, W., Zhu, H., Liu, M., 2023. Structural MRI harmonization via disentangled latent energy-based style translation, in: *International Workshop on Machine Learning in Medical Imaging*, Springer. pp. 1–11.
- Xiao, Z., Kreis, K., Kautz, J., Vahdat, A., 2020. VAEBM: A symbiosis between variational autoencoders and energy-based models. *arXiv preprint arXiv:2010.00654*.
- Zhao, Y., Chen, C., 2021. Unpaired image-to-image translation via latent energy transport, in: *IEEE/CVF Conference on Computer Vision and Pattern Recognition*, pp. 16418–16427.
- Zhu, J.Y., Park, T., Isola, P., Efros, A.A., 2017. Unpaired image-to-image translation using cycle-consistent adversarial networks, in: *IEEE International Conference on Computer Vision*, pp. 2223–2232.
- Zuo, L., Dewey, B.E., Liu, Y., He, Y., Newsome, S.D., Mowry, E.M., Resnick, S.M., Prince, J.L., Carass, A., 2021. Unsupervised MR harmonization by learning disentangled representations using information bottleneck theory. *NeuroImage* 243, 118569.
- Zuo, L., Liu, Y., Xue, Y., Han, S., Bilgel, M., Resnick, S.M., Prince, J.L., Carass, A., 2022. Disentangling a single MR modality, in: *MICCAI Workshop on Data Augmentation, Labelling, and Imperfections*, Springer. pp. 54–63.